CrossMark

Cloud and radiative heating profiles associated with the boreal summer intraseasonal oscillation

Jinwon Kim[1] · Duane E. Waliser[1,2] · Gregory V. Cesana[2,3] · Xianan Jiang[1] ·
Tristan L'Ecuyer[4] · J. M. Neena[5]

Abstract The cloud water content (CW) and radiative heating rate (QR) structures related to northward propagating boreal summer intraseasonal oscillations (BSISOs) are analyzed using data from A-train satellites in conjunction with the ERA-Interim reanalysis. It is found that the northward movement of CW- and QR anomalies are closely synchronized with the northward movement of BSISO precipitation maxima. Commensurate with the northward propagating BSISO precipitation maxima, the CW anomalies exhibit positive ice (liquid) CW maxima in the upper (middle/low) troposphere with a prominent tilting structure in which the low-tropospheric (upper-tropospheric) liquid (ice) CW maximum leads (lags) the BSISO precipitation maximum. The BSISO-related shortwave heating (QSW) heats (cools) the upper (low) troposphere; the longwave heating (QLW) cools (heats) the upper (middle/low) troposphere. The resulting net radiative heating (QRN), being dominated by QLW, cools (heats) the atmosphere most prominently above the 200 hPa level (below the 600 hPa level). Enhanced clouds in the upper and middle troposphere appears to play a critical role in increasing low-level QLW and QRN. The vertically-integrated QSW, QLW and QRN are positive in the region of enhanced CW with the maximum QRN near the latitude of the BSISO precipitation maximum. The bottom-heavy radiative heating anomaly resulting from the cloud-radiation interaction may act to strengthen convection.

Keywords BSISO · Radiative heating · Cloud water · Precipitation · Asian monsoon · Predictability

1 Introduction

Intraseasonal oscillations (ISOs) in the tropics, most prominently the eastward-propagating Madden-Julian Oscillation (MJO) (Madden and Julian 1971) and the northward propagating boreal summer Intraseasonal oscillation (BSISO) (e.g., Yasunari 1979), play crucial roles in shaping the tropical climate. The northward propagating BSISO is of special relevance as it is closely related to the active- and break phases of Asian summer monsoon rainfall (e.g. Lawrence and Webster 2002; Waliser 2006), and thus directly affects over a billion populations in South Asia alone. Hence, understanding of the structure and northward propagation of BSISOs and the skill of numerical models in simulating them have been subjects of intense research (Goswami and Xavier 2003; Waliser et al. 2003; Jiang et al. 2004, 2011a; Abhik et al. 2013; Neena et al. 2016).

Analyzing the cloud water contents (CW) from Cloud-Sat retrievals (Stephens et al. 2008) and winds in the ERA-Interim reanalysis (Dee et al. 2011), Jiang et al. (2011a) found that the meridional-vertical structure of northward propagating BSISOs closely resembles the typical structure of MCSs with positive liquid CW (LCW) and ice CW

✉ Jinwon Kim
jkim@atmos.ucla.edu

1 Joint Institute for Regional Earth System Science and Engineering, University of California Los Angeles, Los Angeles, CA, USA

2 Jet Propulsion Laboratory, California Institute of Technolpgy, Pasadena, CA, USA

3 Present Address: Department of Applied Physics and Mathematics, Columbia University, and NASA Goddard Institute for Space Studies, New York, NY, USA

4 Department of Atmospheric and Oceanic Sciences, University of Wisconsin-Madison, Madison, WI, USA

5 Indian Institute of Science Education and Research, Pune, India

(ICW) anomalies to the north and south of the precipitation maximum in the lower- and upper troposphere, respectively, leading to a tilted structure of the cloud field with height. The lower-tropospheric LCW anomalies may correspond to the planetary boundary layer (PBL) moisture convergence (Jiang et al. 2011a; Abhik et al. 2013) associated with the northward displacement of positive barotropic vorticity anomalies (Jiang et al. 2004). Because of their critical role in the atmospheric radiative transfer processes, the BSISO-related CW structure is expected to lead to a unique radiative heating structure in the region of active BSISO.

Diabatic heating is related with intraseasonal eddy kinetic energy variability and eddy-synoptic flow interactions associated with ISO-related tropical convection, and affects the movement of large-scale circulation anomalies associated with ISOs (Madden and Julian 1971; Salby and Hendon 1994; Lin and Mapes 2004). Radiative heating (QR), along with latent heating and eddy heat fluxes, represent key diabatic heating processes. Clouds play a crucial role in the atmospheric radiative transfer processes which in turn affect the evolution of Indian summer monsoon (Johansson et al. 2015). Hence QR associated with BSISO, in conjunction with CW, is important for understanding the energetics and propagation features of the BSISO. Moreover, identifying the observed structures of the CW and QR anomalies related to BSISO can provide a critical benchmark for evaluating and improving models in parameterized moist convection that play a critical role in simulating the Asian monsoon variability (e.g., Del Genio and Chen 2015).

Despite their importance, there exist only a limited number of studies which analyzed the QR associated with tropical ISOs based on observations or observation-inferred calculations. Lin and Mapes (2004), Ma and Kuang (2011), Jiang et al. (2011b), and Del Genio and Chen (2015) analyzed active MJOs to provide observed structures of QR and CW using data from various sources including a surface Atmospheric Radiation Measurement (ARM) site, CloudSat retrievals, TRMM data and other analysis products. However, no such analysis has appeared for BSISOs. Because MJOs propagate along the equatorial channel while BSISOs propagate from the Equator towards the higher latitudes, convective systems associated with BSISOs are subject to different large scale environments from those for MJOs, especially in the ambient vertical wind shear that strongly affect the structure and northward movements of BSISO (e.g., Jiang et al. 2004; Kang et al. 2010). Thus, applicability of the findings from previous analyses of MJO structures to the structure of BSISOs has not been established.

This study analyzes the meridional-vertical structure of CW and QR anomalies associated with northward propagating BSISOs using the ICW and LCW data from

CloudSat, one of the Afternoon Constellation (A-Train), as well as the shortwave (SW) and longwave (LW) heating rates (QSW and QLW, respectively) derived from the A-train data and ancillary atmospheric variables in the ERA-Interim reanalysis. This is the first time these observational data are used to elucidate the radiative heating structures associated with BSISOs.

2 Data preparation

This study employs the daily precipitation data derived from the Version 7 Tropical Rainfall Measuring Mission (TRMM) Multi-satellite Precipitation Products 3B42 (TRMM7: Huffman et al. 2007) for the period 1998–2014 to identify the northward propagating BSISO events over the tropical Indian Ocean. The TRMM7 data are available for 1998–present; this study uses only up to 2014 as this study began in 2015. The 0.25° TRMM7 data are re-gridded to a 1° × 1° grid by simple averaging of the original 0.25°-resolution data that are located within the area of individual 1° × 1° grids so that they are consistent with the gridded cloud condensates and radiative heating data from CloudSat measurements. The resolution of the analysis grid, 1° × 1°, has been selected to avoid too many CloudSat grid points with missing values for CW and/or QR.

The CW, separately for ice- and liquid phase particles, and QR data based on the CloudSat Radar in Release 4 of the 2B-CWC-RO products (Austin et al. 2009) are gridded into a 1° × 1° × 100 hPa grid nest using the geopotential height-pressure relationship obtained from the ERA-Interim reanalysis. The daily-mean value of ICW and LCW for a grid box is calculated by simply averaging corresponding values within the grid box from all soundings on the given day.

The QR data, both QLW and QSW, are derived from the Release 04 CloudSat 2B-FLXHR-LIDAR dataset. The radiative heating rates are calculated using a broadband radiative transfer model that incorporates the cloud properties retrieved from the CloudSat Profiling Radar, the Cloud-Aerosol Lidar and Infrared Pathfinder Satellite Observation (CALIPSO), and the Moderate Resolution Imaging Spectroradiometer (MODIS), in conjunction with ancillary atmospheric variables from the ECMWF reanalysis (Henderson et al. 2013; L'Ecuyer et al. 2008). Because of limited sampling frequency of CloudSat for properly representing the large diurnal variations of the TOA insolation as well as the critical dependence of the magnitude of QSW on the TOA insolation, using instantaneous QSW values can lead to large errors in representing the daily-mean QSW values (Johansson et al. 2015). In order to alleviate this problem in estimating the daily-mean QSW from CloudSat, the instantaneous QSW values in

CloudSat sounding are normalized by the daily-mean TOA insolation following the methodology in Johansson et al. (2015). For more details of the methodology for normalizing QSW, readers are referred to Johansson et al. (2015; their Eqs. 1–6) and Liou (2002, Sect. 2.2.3). Because of relatively small diurnal variations, the CloudSat QLW data are not scaled. The scaled QSW data and unscaled QLW data are gridded in the same way as the ICW and LCW data described above. Note that the analysis in this study is limited to the period 2006–2010 due to observed data availability because collocation of CloudSat (radar) and CALIPSO (lidar) data became no longer possible after April 2011 when CloudSat experienced battery anomalies. More details of the CloudSat data can be found in the web site: http://www.cloudsat.cira.colostate.edu/data-products/level-2b/2b-flxhr-lidar?term=38.

3 Identification of BSISO events

Northward propagating BSISOs in the summer months from June to September (JJAS) are identified from the TRMM7 daily precipitation data for the period 1998–2014. The 1° × 1°-resolution TRMM7 data prepared in Sect. 2 are first averaged over the Bay of Bengal (BoB) sector, 80°E–95°E, to obtain 1°-resolution meridional distributions of daily precipitation versus day. The resulting daily precipitation data are Lanczos band-pass filtered to isolate ISOs of 20–70 day periods (Jiang et al. 2011a). The latitude-time Hovmöller diagram of the band-pass filtered TRMM7 daily precipitation (Fig. 1) clearly show northward propagating precipitation anomalies over the BoB sector.

Strong BSISO events and their phases are identified by subjecting the filtered daily precipitation anomalies to an extended empirical orthogonal (EEOF) analysis with 21 temporal lags of 1-day intervals. This procedure for identifying the northward moving BSISOs is identical to that in Jiang et al. (2011a) except for the precipitation data (TRMM7 instead of TRMM6) and the period of analysis (1998–2014 instead of 1998–2008). Following the preceding study, strong northward propagating BSISO events are identified by selecting the PC1 time series peaks exceeding 0.8. Seventeen northward propagating BSISOs are identified in this analysis for the summers of 2006–2010 (Fig. 2a–e). For the summers of 2006–2008, the analysis in this study yields nearly identical PC1 time series as well as the precipitation anomaly composite over the ten BSISO events as obtained in Jiang et al. (2011a).

The precipitation anomaly composite of 17 BSISO events for the five summers of 2006–2010 identified from the EEOF analysis (Fig. 3) clearly depicts the northward propagating precipitation anomalies at the speed of
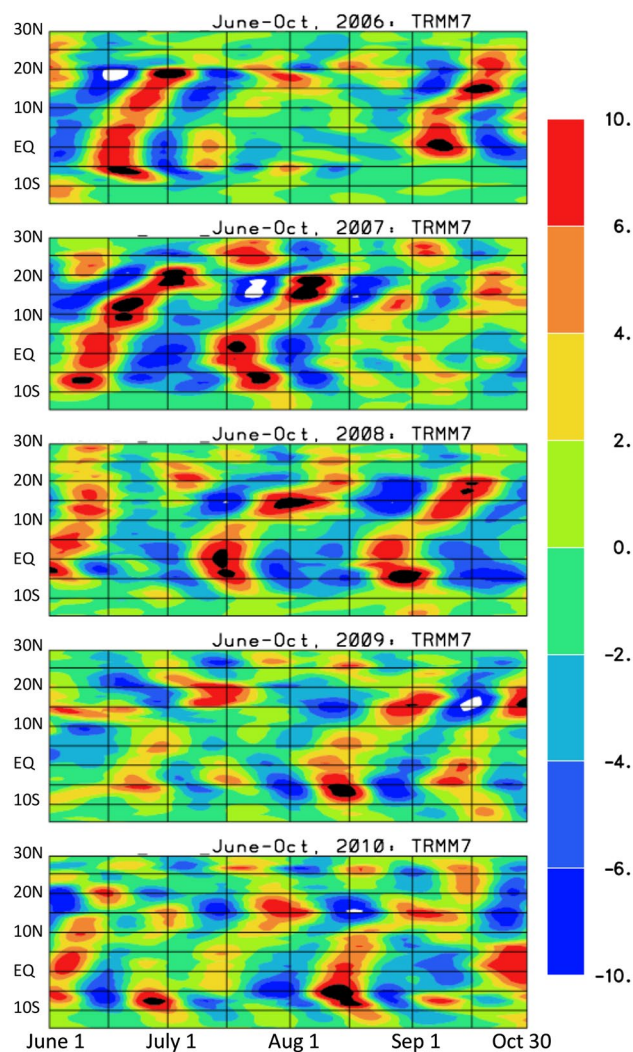

Fig. 1 The Hovmöller diagram of band-pass filtered TRMM daily precipitation (mm/day) for the summers (June–September) of 2006–2010

approximately 1°-latitude/day, similar to the findings in Jiang et al. (2011a) for the three summers of 2006–2008 (see their Fig. 2). Note that the 10 BSISO events for 2006–2008 in this study coincide exactly with those identified in Jiang et al. (2011a, b), This ensures that the BSISO events identified in this study are consistent with those in the previous study. In addition, the larger sample size in this study, 17 northward propagating BSISO events, is more favorable for obtaining statistically robust results than the preceding study of Jiang et al. (2011a) that includes ten events. Construction of the meridional profiles of CW and QR relative to the precipitation maximum as they propagate poleward from the equator to South Asia based on these 17 BSISO events is presented in the following section.
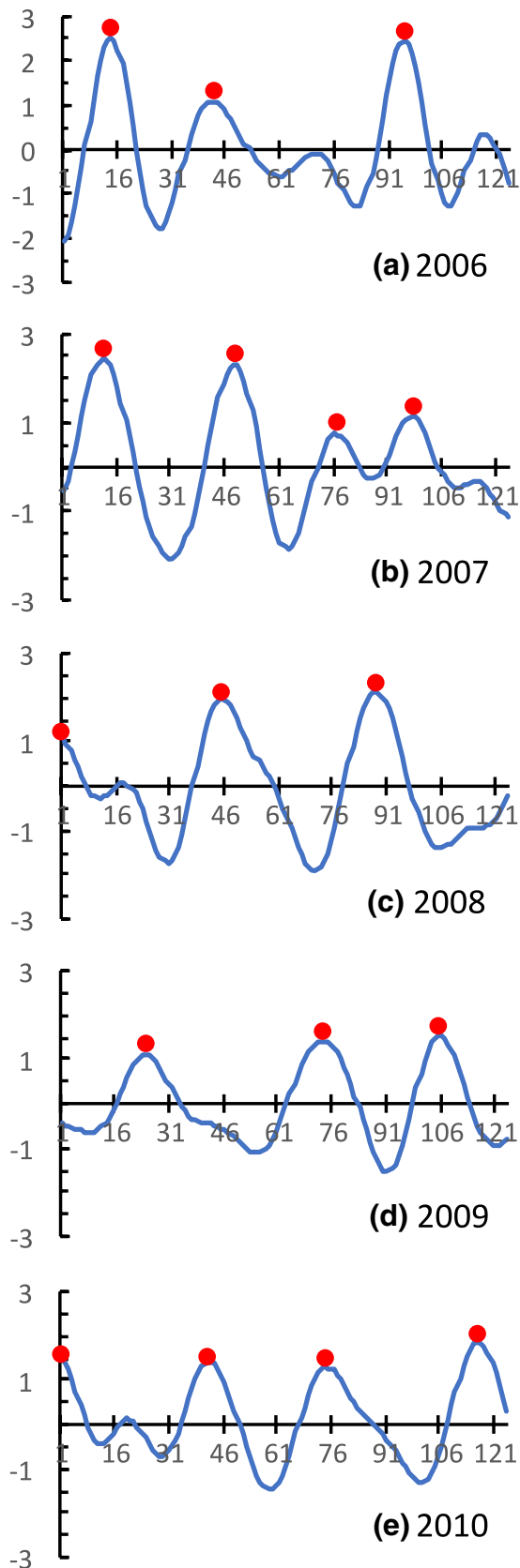
(a) 2006

(b) 2007

(c) 2008

(d) 2009

(e) 2010

Fig. 2 Fig. 2 The PC1 time series of the band-pass filtered TRMM daily precipitation for the summers (June–September) of 2006–2010. The *red dots* indicate the strong northward propagating BSISO events
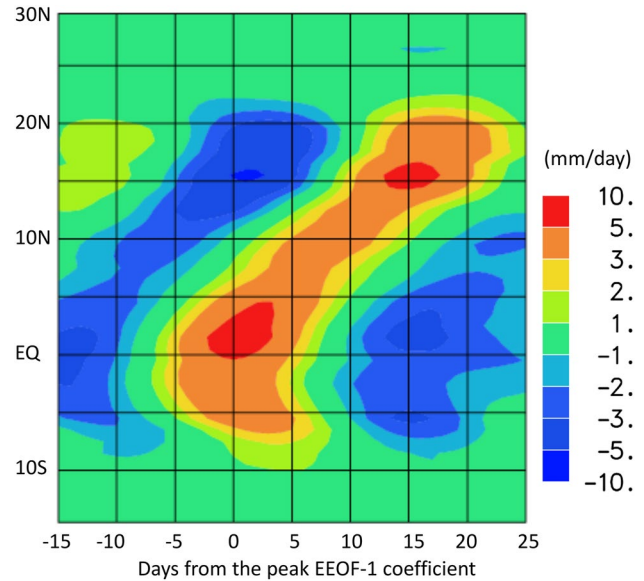

Fig. 3 The Hovmöller diagram of composite precipitation anomalies for the 17 strong northward propagating BSISO events in the period 2006–2010

4 The BSISO CW and QR during northward propagations

Estimates of CW, both ICW and LCW, from the CloudSat Radar in Release 4 of the 2B-CWC-RO products (Austin et al. 2009) are used to calculate the CW anomalies over the BoB sector for the 17 BSISO events. Instead of band-pass filtering, the CW anomalies corresponding to these BSISO events are calculated against their climatology for the summer period (June–September) due to a large amount of missing data (Jiang et al. 2011a). The ICW and LCW anomalies are smoothed temporally and spatially by block averaging over 5-day periods and 5° in latitudes, respectively. Anomaly composites of CW and daily precipitation for the days of peak PC1 (Day00) and 5-day intervals thereafter in Fig. 4 clearly show northward propagating CW anomalies in conjunction with the northward movement of the precipitation maximum. The meridional-vertical cross-section of the BSISO-related CW field in Fig. 4 are characterized by positive LCW (ICW) anomalies in the lower (upper) troposphere that lead (lag) the positive peak precipitation anomalies as found in Jiang et al. (2011a). The positive low-level LCW peak is related to the low-level convergence to the north of the positive peak precipitation that accompanies prevailing shallow cumulus clouds (Jiang et al. 2011a; Abhik et al. 2013). The upper tropospheric positive ICW maximum is due to the enhanced cirrus clouds from deep convection over the precipitation maximum and the detrainment of ice crystals by upper-level northerly outflow relative to the precipitation maximum.
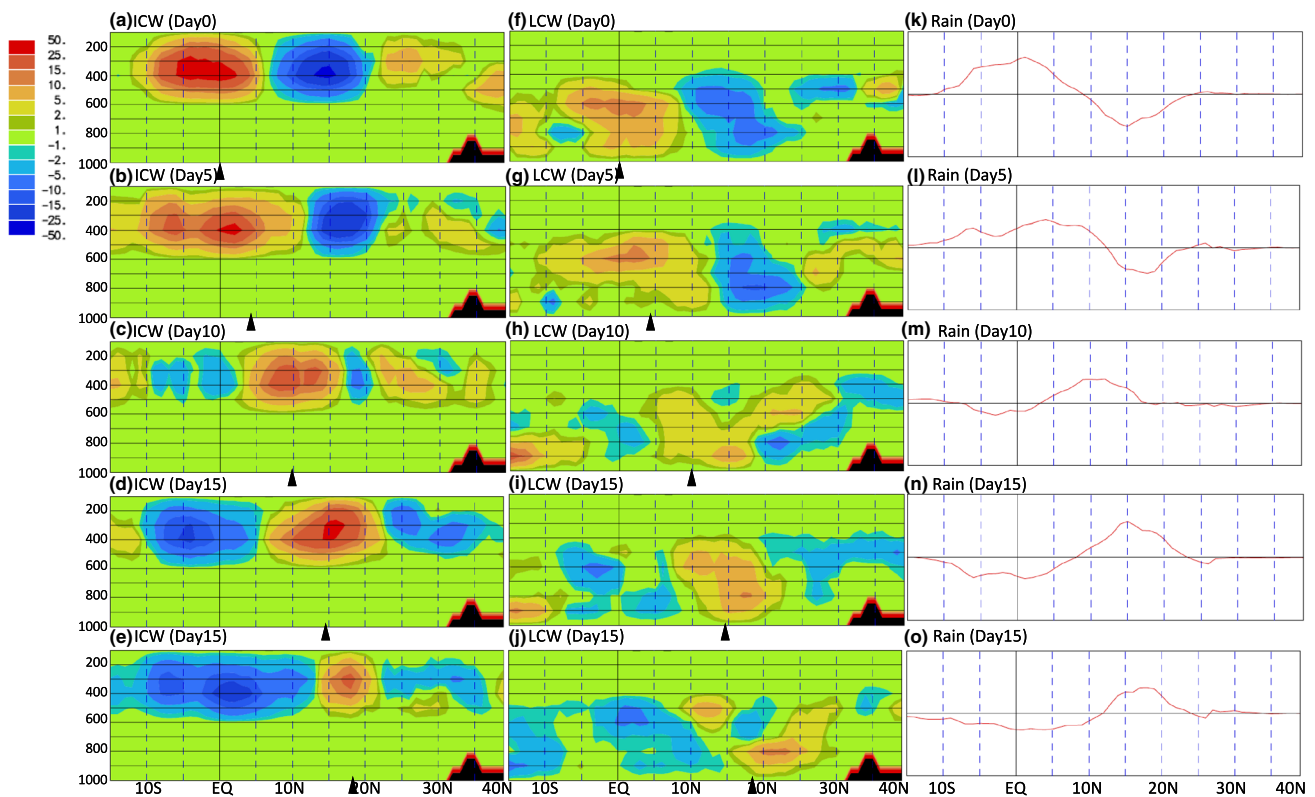
Fig. 4 The meridional-vertical cross-sections of the composite ice (**a–e**) and liquid (**f–j**) phase cloud water content anomalies on the days of 0, 5, 10, 15, and 20 during northward propagation after the day of peak PC1 coefficients in Fig. 2a–e. Figure 4k–o are the corresponding precipitation anomalies. The *black wedges* in **a–j** indicates the location of the positive rainfall peak

The upper-level northerly outflows relative to the latitude of precipitation maximum are clearly depicted in the BSISO-related composite of wind anomalies in Jiang et al. (2011a; their Fig. 9a). This results in southward tilting with height in the positive CW anomalies.

Temporal evolutions of the equivalent composites of the BSISO-related QR anomalies from the Release 04 CloudSat 2B-FLXHR-LIDAR dataset are presented in Fig. 5. Similar to the temporal variations in the BSISO-composite CW, the BSISO-related QSW (Fig. 5a–e) and QLW (Fig. 5f–j) anomalies propagate towards the north in conjunction with the northward movement of the positive precipitation peak (Fig. 5k–o). A positive QSW maximum occurs in the upper part of the positive ICW anomaly (150–300 hPa) and is paired with a negative QSW peak in the lower troposphere below the 800 hPa level (Fig. 5a–e). The QLW anomalies (Fig. 5f–j) are characterized by a negative peak near the top of the positive ICW anomaly (100–200 hPa), immediately above the upper-level positive QSW maximum, and a low tropospheric (800–900 hPa) positive peak beneath the negative QLW peak in the upper troposphere. This structure of QSW and QLW is maintained during the course of the northward propagation. Figures 4 and 5 also show that the northward movement of

QR and CW are closely synchronized with the northward propagation of the positive precipitation peak.

5 CW and QR structures relative to the peak precipitation latitude

To examine the meridional-vertical structure of the BSISO-related QR and CW structures corresponding to the meridional variations in precipitation, the BSISO-related anomalies of ICW, LCW, QSW, QLW and precipitation during the course of strong northward propagation (days from 5 to 22 after the onset of each BSISO event) of the 17 BSISO events are composited with respect to the relative latitude about the peak precipitation anomalies (Fig. 6). The composite CloudSat ICW anomalies (Fig. 6a) are characterized by a large region of enhanced ice clouds by 15–25 mg m^{-3} in the upper troposphere (around 350 hPa) that lags (i.e., located to the south of) the precipitation maximum by 1–2° in latitude. The composite LCW anomalies (Fig. 6b) are characterized by two positive peaks of 5–10 mg m^{-3}; the LCW peak at 850 hPa leads the peak precipitation (Fig. 6d) by 2° in latitudes and the one at 600 hPa lags the peak precipitation by 3° in latitudes. The low-level LCW maximum
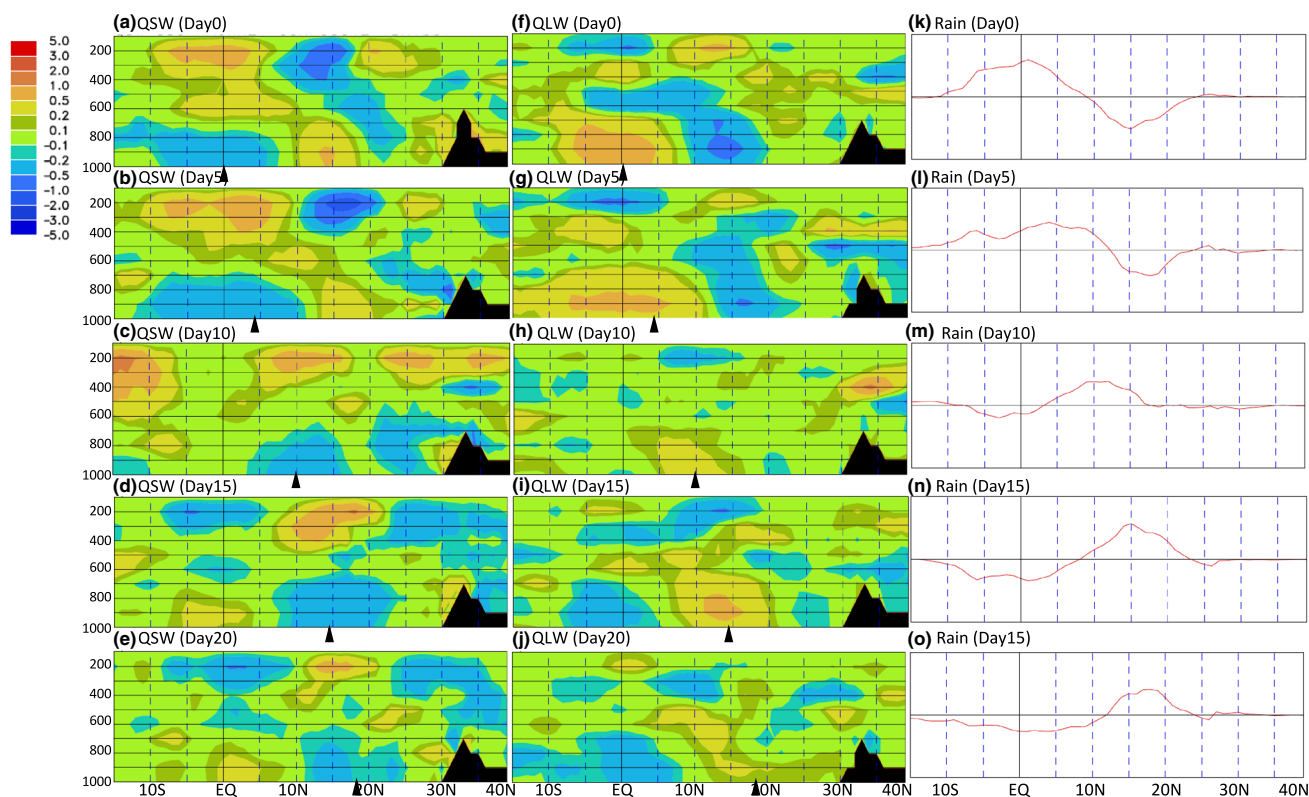
Fig. 5 The meridional-vertical cross-sections of the composite QSW (**a–e**) and QLW (**f–j**) anomalies on the days of 0, 5, 10, 15, and 20 during northward propagation after the day of peak PC1 coefficients

in Fig. 2a–e. **k–o** are the corresponding precipitation anomalies. The *black wedges* in **a–j** indicates the location of the positive rainfall peak

corresponds to the low-level convergence ahead of the precipitation maximum (Jiang et al. 2011a; Abhik et al. 2013; Kang et al. 2010). Note that the 10 BSISO events for 2006–2008 in Jiang et al. (2011a) exactly correspond to those in this study for the same period. Because of this, we assume that the structure of wind fields presented in Jiang et al. (2011a) also applies to the 17 samples for 2006–2010 analyzed in this study without further analyses. The mid-tropospheric (600 hPa) LCW maximum near the freezing level may be related to melting snow/ice particles (Houze Jr. 2004). Structures of the ICW and LCW anomalies found in this study compare well with Jiang et al. (2011a) except that the mid-tropospheric LCW maximum stands out more strongly in this study. Overall, the meridional-vertical cross-section of the composite anomalies of CW obtained in this study, in conjunction with the wind fields found in Jiang et al. (2011a), resemble closely an idealized tropical oceanic MCS with leading-line/trailing stratiform structure (Houze Jr. 2004; Zipser 1977).

The composite QSW (Fig. 6e) is characterized by a positive peak of 0.2–0.3 K day^{-1} around the 200 hPa level, near the top of the upper tropospheric positive ICW anomaly, and a negative peak between −0.1 and −0.2 K day^{-1} near the surface. The positive QSW maximum in the upper

troposphere indicate enhanced SW absorption by increased ICW in the upper part of the ice cloud layers. The lower tropospheric negative QSW is likely the result of shading by the enhanced CW in the upper- and middle levels (Fig. 4c). The BSISO-related QLW structure (Fig. 6f) shows a deep layer of low-tropospheric (900 hPa) heating of 0.4–0.5 K day^{-1} accompanied by a shallow layer of cooling by 0.3–0.4 K day^{-1} in the upper troposphere (200 hPa). The positive QSW peak and the negative QLW peak in the upper troposphere in Fig. 6e, f resemble the cloud radiative heating structure in the upper troposphere for the Indian monsoon period reported in Johansson et al. (2015). The low-level QLW maximum occurs immediately below the total CW (TCW; ICW + LCW) maxima in the middle and low troposphere (Fig. 6c), perhaps due to the absorption of downwelling LW fluxes from the increased upper- and mid-level clouds by the enhanced low-level clouds. The role of enhanced downwelling LW fluxes from the increased upper-level clouds in enhancing the low-level QLW may be further supported by the fact that the positive QLW peak is located immediately below the positive upper-level TCW maxima trailing the peak precipitation, not at the low-level positive TCW maxima leading the precipitation maximum.

Fig. 6 The meridional-vertical cross-sections of the composite cloud water (**a**–**c**) and radiative heating rate (**e**, **f**) anomalies with respect to the latitude of maximum precipitation shown in **d**. Also shown is the vertically integrated net radiative heating rate (**h**)
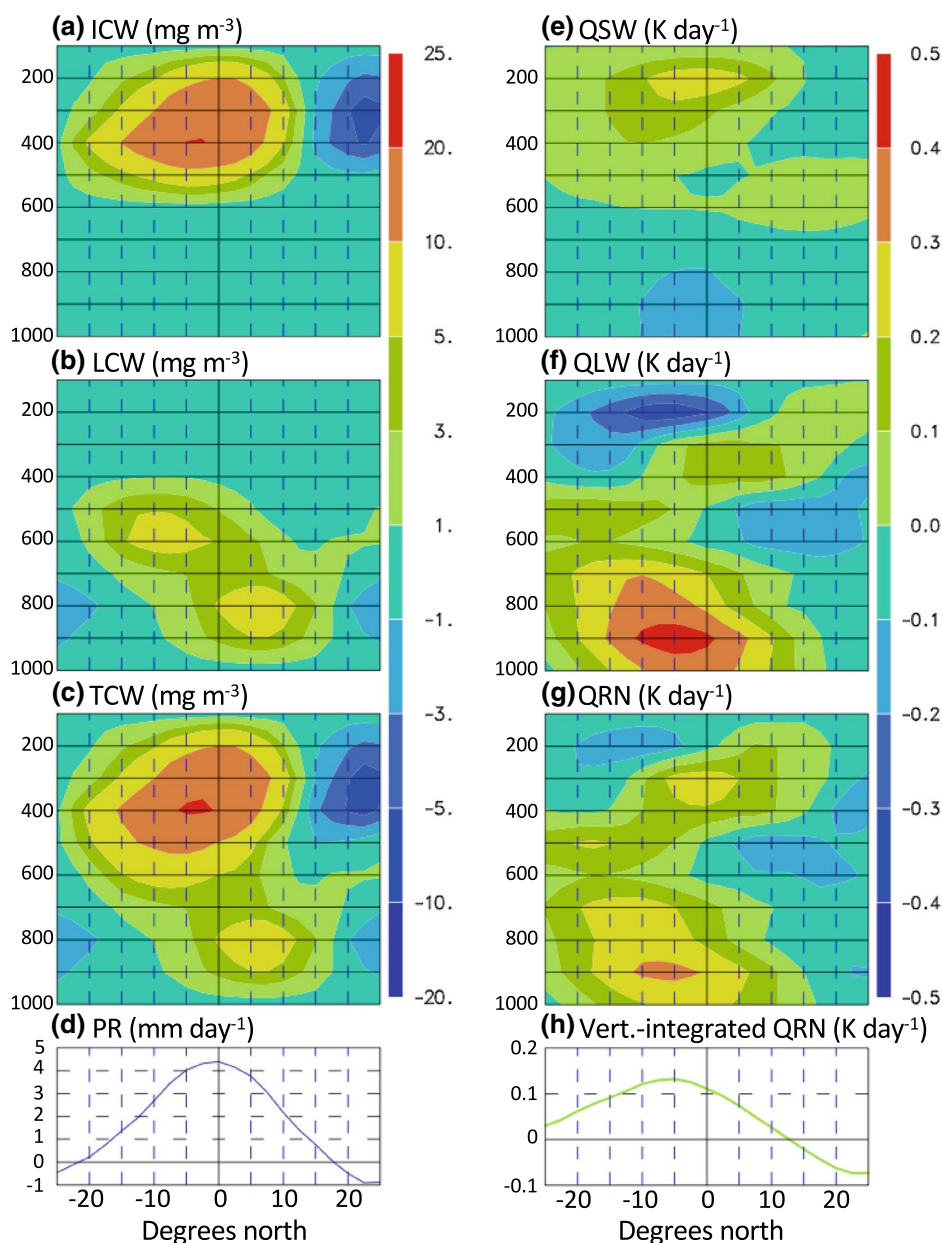
The vertical structure of QSW, positive in the upper troposphere and negative in the lower troposphere, is opposite to QLW, with QLW of larger magnitudes than QSW. Similar structures in the radiative heating anomalies for MJOs are also reported from the analyses of A-train data by Del Genio and Chen (2015). As a consequence, net radiative heating rate (QRN) anomalies (Fig. 6g) largely resemble the QLW in Fig. 6f, and are characterized by two positive maxima; one located at 2–4° to the south of the precipitation maximum in the low level (about 900 hPa) and one above the precipitation maximum in the upper level, around the 350 hPa level. Shallow negative QRN peak also appear around the 200 hPa level, between 2° and 8° to the south of the peak precipitation latitude. This upper tropospheric

negative QRN peak is consistent with a kinetic modeling study of tropical cloud clusters by Churchill and Houze Jr. (1991). Note that the scaling of instantaneous QSW to take into account the diurnal variations on the insolation is essential for obtaining the daily-mean QR fields because, at each location, atmospheric profiles from CloudSat are available only at certain times of the day (Johansson et al. 2015).

For better understanding of the QR associated with the strong northward propagating BSISOs, the horizontally-averaged (Fig. 7a) and vertically-integrated (Figs. 7b, 6h) radiative heating rate anomalies are examined. The vertical profiles in Fig. 7a are obtained by averaging the corresponding radiative heating anomalies (Fig. 6e–g) over the
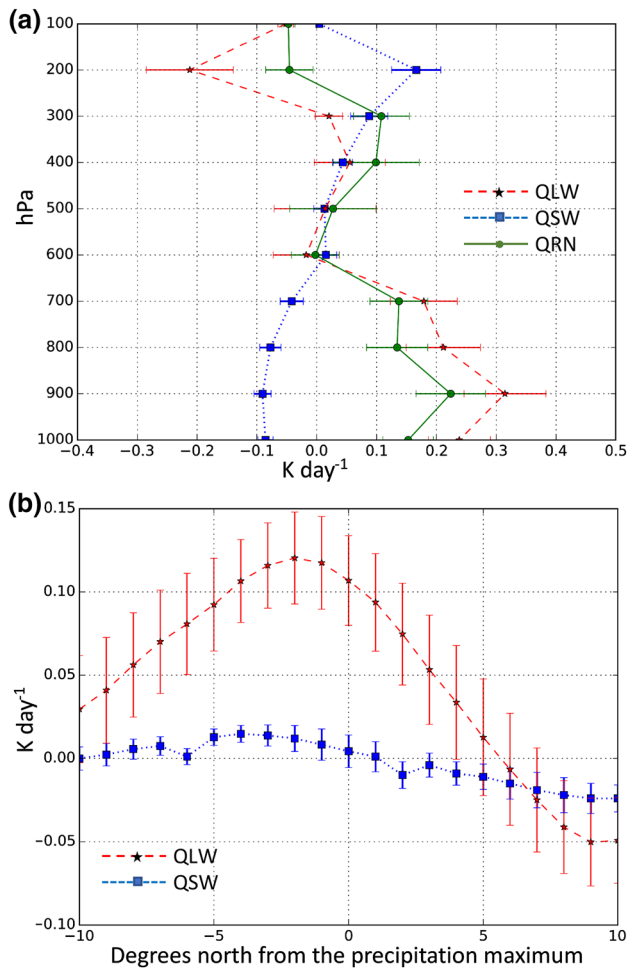
Fig. 7 a The vertical profiles of the radiative heating anomalies averaged meridionally from $-8°$ to $+5°$ from the latitude of maximum precipitation and **b** the meridional distribution of the vertically-integrated QSW and QLW anomalies relative to the latitude of precipitation maximum. *Error bars* in **a** and **b** indicate the 95% confidence interval based on the two-sided Student's *t* test

latitude range of significant CW anomalies, from $-8°$ to $5°$ in latitudes relative to the precipitation maximum. The BSISO-related QSW (squares with blue dashed line) heats the upper troposphere, above the 600 hPa level, and cools the lower troposphere below that level. The QLW anomalies (stars with red dashed line) show opposite effects with cooling/heating in the upper/lower troposphere around the same pressure level (600 hPa). In the upper troposphere, both positive QSW and negative QLW peak at the 200 hPa level (Fig. 7a), near the top of the enhanced ICW (Fig. 6a). In the lower troposphere, both the negative QSW and positive QLW peaks appear at the 900 hPa level. In the lower troposphere, the vertical variation in QLW is much smoother than that in QSW (Fig. 7a). Magnitudes of both QSW and QLW anomalies are smallest in the middle troposphere, from 500 to 600 hPa, near the melting level where

transition from LCW to ICW occurs as can be inferred from Fig. 6a, b. The vertical variations in QRN (circles with green solid line) are dominated by QLW with a deep layer of heating below the 200 hPa level and a shallow layer of cooling above that level. Thus, the vertical variations in the QRN anomalies tend to destabilize the cloud column, especially in the upper part of the enhanced ice clouds as reported in Churchill and Houze Jr. (1991). The vertical distribution of these radiative heating rate anomalies is similar to that found for (boreal winter, eastward propagating) MJOs in Ma and Kuang (2011) except for some details such as the mid-tropospheric QRN minima for the BSISO found in this study.

The vertically-integrated BSISO-related radiative heating in the region of enhanced CW (Figs. 7b, 6g) show that the QRN anomalies are primarily determined by QLW. Both vertically-integrated QSW and QLW anomalies are positive in the region of significant cloud cover. That is, the radiative effects of enhanced clouds tend to reduce LW cooling and enhance SW heating compared to the clear-sky condition, but the reduction in LW cooling dominates the increase in SW heating. The resulting bottom-heavy QRN profile with the positive column-integrated QRN (Figs. 6g, 7a) can work towards strengthen convection as discussed in Kuang (2011), Ma and Kuang (2011), and Wolding et al. (2016). The magnitude of QRN anomalies (Fig. 7b) generally follow the amount of TCW anomalies (Fig. 6c) with the maximum positive QRN lagging the precipitation maximum by about $2°$. The dominance of QLW in QRN and the occurrence of the positive peak QRN anomaly close to the precipitation maximum are also documented in an observational study of the MJO by Lin and Mapes (2004). The QRN anomalies turn into negative in the region to the north of $+5°$ from the precipitation maximum where the TCW anomalies become negative or negligible (Fig. 6c).

6 Summary and conclusions

Structures of anomalous CW and QR corresponding to 17 strong northward propagating BSISO events for the period 2006–2010 are analyzed using data from A-Train satellite observations in conjunction with the geopotential height-pressure relationship from the ERA-Interim reanalysis and TRMM7 daily precipitation data. All data are gridded onto a $1° \times 1°$ (2-dimensional fields) or $1° \times 1° \times 100$ hPa (3-dimensional fields) grid nests. Northward moving BSISO events are identified from the EEOF analysis of 20–70-day band-pass filtered TRMM7 daily precipitation data averaged over the BoB longitude sector. The band-pass filtered as well as the BSISO-composite TRMM7 precipitation show clearly-defined northward propagating daily precipitation anomalies at speeds of $1°$-latitude day^{-1}.

The composite BSISO-related CW profiles exhibit an anomalous ICW maximum centered at the 350 hPa level and 2° to the south of the latitude of peak precipitation, and two LCW maxima, one at 850 hPa located 2° to the north of the peak precipitation and one at 600 hPa located 3° to the south of the precipitation maximum. The upper-level positive ICW peak is located immediately above and slightly downstream of the BSISO-precipitation maximum, and is due to enhanced convection and the transport of the resulting ICW by the upper-level northerly outflows that were identified in a previous study (Jiang et al. 2011a). The low-level LCW maximum may be related to shallow cumulus clouds associated with the low-level convergence ahead of the MCS (Abhik et al. 2013) while the mid-level LCW peak, located near the freezing level, could be due to the melting of ice particles falling from the anvil. The structure of the BSISO-related CW found in this study closely resembles that found in Jiang et al. (2011a) for a shorter period 2006–2008 based on a smaller number (10) of samples. Because the 10 samples for 2006–2008 in Jiang et al. (2011a) exactly correspond to those in this study for the same period, we assume that the BSISO-related wind structures presented in Jiang et al. (2011a) also apply to the 17 samples for 2006–2010 in this study without further analyses.

The northward propagation of the composite anomalies of ICW, LCW, and radiative heating rates are closely synchronized with the northward movement of the BSISO-precipitation peak. Associated composite QRN anomalies peak at about 2° to the south of the precipitation maximum where upper-level ICW maxima occur, and are dominated by QLW with some modulation by QSW. The net radiative heating cools (heats) the troposphere above (below) the 200 hPa level. The composite BSISO-related radiative heating structure also shows: (1) positive (negative) QSW peak of about 0.3 K day^{-1} (−0.2 K day^{-1}) in the upper (lower) troposphere, (2) negative QLW peak up to −0.5 K day^{-1} at 200 hPa to the south of the precipitation maximum, and (3) positive low-level QLW maxima of up to 0.4 K day^{-1} around the 900 hPa level 2–4° to the south of the precipitation maximum.

Vertical profiles of the horizontally-averaged BSISO-related QR show that QSW warm (cool) the upper (lower) troposphere. Vertical variations in the horizontally-averaged QLW show opposite effects from the QSW effects, i.e., cool (warm) the upper (lower) troposphere. Effects of the net radiative heating result in overall warming of the troposphere, especially the lower part of it, except cooling of a shallow layer in the upper troposphere near the top of the enhanced ice cloud layer. The shallow upper-level cooling mainly work to destabilize the top of the cirrus (ice cloud) layer. Integrated vertically over the entire troposphere, QRN is positive within the BSISO precipitating region with the maximum occurring about 2° to the south of the peak precipitation latitude, similarly as in Lin and Mapes (2004) for an active MJO. The column-integrated QSW and QLW are both positive within the BSISO precipitating region of enhanced CW. The longwave heating rate, QLW, is substantially larger than QSW. Thus, QRN is essentially determined by QLW as found for MJOs by Del Genio and Chen (2015) from analyses of A-train data. The bottom-heavy QRN anomalies show that the BSISO-related radiative heating may work towards strengthening convection (Kuang 2011; Wolding et al. 2016).

The BSISO-related CW and QR structures obtained in this study, as well as the CW structure found in Jiang et al. (2011a), show notable differences from those for active MJOs reported in Ma and Kuang (2011). The most noticeable differences between the BSISO- and MJO-related structures are in the vertical tilting of CW and the altitude where the maximum CW and QR appears. The BSISO-related CW anomalies in this study and Jiang et al. (2011a) show a bimodal distribution in the vertical with maxima in the upper and lower troposphere separated by mid-tropospheric minima (Fig. 6c) while the MJO composite in Ma and Kuang (2011) show peak positive CW anomalies in the middle troposphere. Both the BSISO-related QRN in this study and the MJO-related QRN in Ma and Kuang (2011) show bi-modal distributions in the vertical, two maxima separated by mid-level minima. The main difference between these two distributions is that the upper-level QR maxima occur in the 300–400 hPa layer for the BSISO and in the 450–550 hPa layer for the MJO. These differences in the CW and QR structures between the BSISO and the MJO may be related to the differences in their large-scale environments, especially the vertical wind shear that significantly affects convective systems. Detailed processes associated with the CW and QR structures associated BSISO and MJO are a subject of future studies.

References

Abhik S, Hadler M, Mukhopadhyay P, Jiang X, Goswami BN (2013) A possible new mechanism for northward propagation of boreal summer intraseasonal oscillations based on TRMM and MERRA reanalysis. Clim Dyn 40:1611–1624

Austin RT, Heymsfield AJ, Stephens AJ (2009) Retrievals of ice cloud microphysical parameters using the CloudSat millimeter-wave radar and temperature. J Geophys Res 114:D00A23

Churchill DD, Houze RA Jr (1991) Effects of radiation and turbulence on the diabatic heating and water budget of the stratiform region of a tropical cloud cluster. J Atmos Sci 48:903–922

Dee DP, Uppala SM, Simmins J, Berriford P, Poli P, Kobayashi S, Andrae U, Balmaseda MA, Balsamo G, Bauer P, Bechtold P, Beljaars ACM, van de Berg L, Bidlot J, Bormann N, Delsol C, Dragani R, Fuentes M, Geer AJ, Haimberger L, Healy SB, Hersbach H, Hólm EV, Isaken L, Kållberg P, Köhler M, Matricardi M, McNally AP, Monge-Sanz BM, Morcrette J, Park B, Peubey C, de Rosnay P, Tavolato C, Thépaut J, Vitart F (2011) The ERA-Interim reanalysis: configuration and performance of the data assimilation system. Quart J Roy Meteor Soc 137:553–597

Del Genio AD, Chen Y. (2015) Cloud-radiative driving of the Madded-Julian oscillations as seen be the A-Train. J. Geophys. Res Atmos 120:5344–5356

Goswami BN, Xavier PK (2003) Potential predictability and extended range prediction of Indian summer monsoon breaks. Geophys Res Lett 30(18):1966

Henderson DS, L'Ecuyer T, Stephens GL, Partain, Sekiguchi M (2013) A multisensory perspective on the radiative impacts of clouds and aerosols. J Appl Meteor Climatol 52:853–871

Houze Jr. RA (2004) Mesoscale convective system. Rev Geophys 42:RG4003

Huffman GJ, Alder RF, Bolvin DT, Gu G, Nelkin EJ, Bowman EP, Hong Y, Stocker EF, Wolff DB (2007) The TRMM multisatellite precipitation analysis (TMPA): quasi-global, multi-year, combined-sensor precipitation estimates at fine scales. J Hydrometeor 8:38–55

Jiang X, Li T, Wang B (2004) Structures and mechanisms of the northward propagating boreal summer intraseasonal oscillation. J Clim 17:1022–1039

Jiang X, Waliser DE, Li J, Woods C (2011a) Vertical cloud structures of the boreal summer intraseasonal variability based on CloudSat observations and ERA-Interim reanalysis. Clim Dyn 36:2219–2332

Jiang X, Waliser DE, Olson WS, Tao W, L'Ecuyer TS, Li K, Yung YL, Shige S, Lang S, Takayabu YN (2011b) Vertical diabatic heating structure of the MJO: intercomparison between recent reanalyses and TRMM estimates. Mon Wea Rev 139:3208–3223

Johansson E, Devasthale A, L'Ecuyer TL, Ekman AML, Tjernström M (2015) The vertical structure of cloud radiative heating over the Indian subcontinent during summer monsoon. Atmos Chem Phys 15:11557–11570

Kang I, Kim D, Kug J (2010) Mechanisms for northward propagation of boreal summer intraseasonal oscillation: convective momentum transport. Geophys Res Lett 37:L24804

Kuang Z (2011) The wavelength dependence of the gross moist stability and the scale selection in the instability of column-integrated moist static energy. J Atmos Sci 68:61–68

L'Ecuyer TS, Wood NB, Haladay T, Stephens GL, Stackhouse PW Jr (2008) Impact of clouds on atmospheric heating based on the R04 CloudSat fluxes and heating rates data set. J Geophys Res 113:D00A15

Lawrence DM, Webster PJ (2002) The boreal summer intraseasonal oscillation: relationship between northward and eastward movement of convection. J Atmos Sci 59:1593–1606

Lin J, Mapes BE (2004) Radiation budget of the tropical intraseasonal oscillation. J Atmos Sci 61:2050–2062

Liou KN (2002) An introduction to atmospheric radiation. Academic Press, 525 B St., Suite 1900, San Diego, California, USA, p 583

Ma D, Kuang Z (2011) Modulation of radiative heating by the Madden–Julian oscillations and convectively coupled Kelvin waves as observed by CloudSat. Geophys Res Lett 38:L20813

Madden RA, Julian PR (1971) Detection of a 40–50 day oscillation in the zonal wind in the tropical Pacific. J Atmos Sci 28:702–708

Neena JM, Waliser DE, Jiang X (2016) Model performance metrics and process diagnostics for boreal summer intraseasonal variability. Clim Dyn 1–23

Salby ML, Hendon HH (1994) Intraseasonal behavior of clouds, temperature, and motion in the Tropics. J Atmos Sci 51:2207–2224

Stephens GL, Vane DG, Tanelli S, Im E, Durden S, Rokey M, Reinke D, Partain P, Mace GG, Austin R, L'Ecuyer T, Haynes J, Lebsock M, Suzuki K, Waliser DE, Wu D, Kay J, Gettleman A, Wang Z (2008) The CloudSat mission: performance and early science after the first year of operation. J Geophys Res 113:d00a18

Waliser DE (2006) Intraseasonal variations. In: Wang B (ed) The Asian monsoon. Springer, Heidelberg, p 787

Waliser DE, Jin K, Kang I, Stern WF, Schubert S, Wu MLC, Lau KM, Lee MI, Krishnamurthy V, Kitoh A, Meehl GA, Galin VY, Satyan V, Mandke SK, Wu G, Liu Y, Park CK (2003) AGCM simulations of intraseasonal variability associated with the Asian summer monsoon. Clim Dyn 21:423–446

Wolding BO, Maloney ED, Branson M (2016) Vertically resolved weak temperature gradient analysis of the Madden-Julian oscillation in SP-CESM. J Adv Model Earth Syst 8. doi:10.1002/2016MS000724

Yasunari T (1979) Cloudiness fluctuation associated with the northern hemisphere summer monsoon. J Meteorol Soc Japan 57:227–242

Zipser EJ (1977) Mesoscale and convective-scale downdraughts as distinct components of squall-line circulation. Mon Wea Rev 105:1568–1589